JMEPEG (2011) 20:877–893
DOI: 10.1007/s11665-010-9724-z

1059-9495/$19.00

Fluid/Structure Interaction Computational Investigation of Blast-Wave Mitigation Efficacy of the Advanced Combat Helmet

M. Grujicic, W.C. Bell, B. Pandurangan, and P.S. Glomski

(Submitted April 4, 2010)

To combat the problem of traumatic brain injury (TBI), a signature injury of the current military conflicts, there is an urgent need to design head protection systems with superior blast/ballistic impact mitigation capabilities. Toward that end, the blast impact mitigation performance of an advanced combat helmet (ACH) head protection system equipped with polyurea suspension pads and subjected to two different blast peak pressure loadings has been investigated computationally. A fairly detailed (Lagrangian) finite-element model of a helmet/skull/brain assembly is first constructed and placed into an Eulerian air domain through which a single planar blast wave propagates. A combined Eulerian/Lagrangian transient nonlinear dynamics computational fluid/solid interaction analysis is next conducted in order to assess the extent of reduction in intra-cranial shock-wave ingress (responsible for TBI). This was done by comparing temporal evolutions of intra-cranial normal and shear stresses for the cases of an unprotected head and the helmet-protected head and by correlating these quantities with the three most common types of mild traumatic brain injury (mTBI), i.e., axonal damage, contusion, and subdural hemorrhage. The results obtained show that the ACH provides some level of protection against all investigated types of mTBI and that the level of protection increases somewhat with an increase in blast peak pressure. In order to rationalize the aforementioned findings, a shockwave propagation/reflection analysis is carried out for the unprotected head and helmet-protected head cases. The analysis qualitatively corroborated the results pertaining to the blast-mitigation efficacy of an ACH, but also suggested that there are additional shockwave energy dissipation phenomena which play an important role in the mechanical response of the unprotected/protected head to blast impact.

Keywords advanced combat helmet, computational analysis, fluid-structure interaction, traumatic brain injury

1. Introduction

Traumatic brain injury (TBI) is generally considered a signature injury of the current military conflicts. Due to the resulting high direct and indirect economic costs to society at large (through lost earning potential of the affected and the burden of care imposed on their families) and life-altering long-term consequences, TBI is becoming an important societal problem. While in the general population, TBI is mostly caused by motor-vehicle accidents involving collision and rollover as well as by sport- and work-related accidents, TBI cases analyzed in the present work, on the other hand, are associated with military personnel exposed to blast and/or ballistic impacts. It is interesting to note that as advanced body armor and head protection gear have greatly reduced soldier fatalities from explosion and ballistic attacks, the problem of TBI in the attack survivors has become more prevalent (Ref 1-3). In particular, the problem of blast-induced TBI, which is typically not accompanied by visible, external bodily injuries, has become a serious problem that demands an urgent solution.

A review of the literature carried out as part of the present work revealed that while impact-induced TBI associated with car crashes, sport- and work-related accidents has been studied extensively and its causes well understood and linked with the acceleration and impact of the head, a similar level of understanding of blast-induced TBI has been lacking (Ref 4, 5). Blast-induced TBIs are typically classified as: (a) primary TBI resulting from the propagation and reflection of blast-induced shock waves within the intra-cranial cavity; (b) secondary TBI caused by the ballistic impact of a person's head with an object propelled by the blast; and (c) tertiary TBI caused by the blast-induced propulsion of a person's head and its subsequent impact against a rigid/hard surrounding structure (Ref 2). In the early days of TBI research, the prevailing opinion was that all TBIs were of a tertiary nature and, consequently, TBI mitigation efforts were mainly focused on reducing the acceleration of the head (Ref 2). However, shock tube experiments involving restrained animal subjects indicated that primary and secondary blast-induced TBIs do occur since TBI was detected even in the absence of any head motions/impact (Ref 6).

TBIs are additionally classified as penetrating (pTBIs) and closed (cTBIs) where the former involves skull penetration/fracture while, in the latter case, structural integrity of the skull

M. Grujicic, W.C. Bell, B. Pandurangan, and **P.S. Glomski**, Department of Mechanical Engineering, Clemson University, 241 Engineering Innovation Building, Clemson, SC 29634-0921. Contact e-mails: mica.grujicic@ces.clemson.edu and gmica@clemson.edu.

is maintained. cTBIs, which are considered in the present work, are further classified as mild (mTBIs), moderate and severe (Ref 7). Often mTBIs are referred to as concussions. Both among civilians and military personnel, pTBIs are primarily associated with ballistics (e.g., gunshot wounds). As far as cTBIs are concerned, among civilians, they are most often related to vehicular, work- and sport- related accidents. On the other hand, cTBIs among military personnel are predominantly associated with exposure to high-intensity air-blast waves.

The most frequently cited mechanisms responsible for the blast-induced TBI are: (a) blast-induced compression of the thorax which causes a vascular surge into the brain (Ref 6) (primary TBI); (b) blast/object-impact induced skull flexure which may create shock waves within the brain comparable in strength to those associated with injury-inducing head impact situations (primary/secondary TBI); (c) shock-wave ingress into the intracranial cavity through skull orifices (primary TBI); and (d) (0 mode) bulk acceleration of the head (Ref 2) (tertiary TBI).

Historically, the main head protection gear has been the helmet. Over the years, the design of military helmets has continuously evolved in order to respond to ever-increasing lethality and diversity of threats, to take advantage of the new materials and fabrication/manufacturing technologies, and to meet continuously growing demands for lower weight and improved comfort. An excellent review of the helmet-design evolution from that used in World War I to those currently used can be found in Ref 8.

For the most part, two helmet designs are currently being used by the US military (Ref 7): (a) the so-called advanced combat helmet (ACH) and (b) the so-called light-weight marine corps helmet (LWH). The ACH helmet design is (described below and) analyzed in the present work. A fairly detailed description of the LWH design can be found in our recent work (Ref 9).

An ACH helmet consists of a 7.8-mm thick outer composite shell based on lower-content phenolic resin reinforced with higher-strength Kevlar 129 fibers, a modified edge cut for lower protection surface and a "suspension system" (a set of discrete foam pads strategically placed on the interior surface of the helmet and held in place by Velcro-based hook-and-loop fasteners). A geometrical model of the ACH helmet, with all its basic components identified, is displayed in Fig. 1.

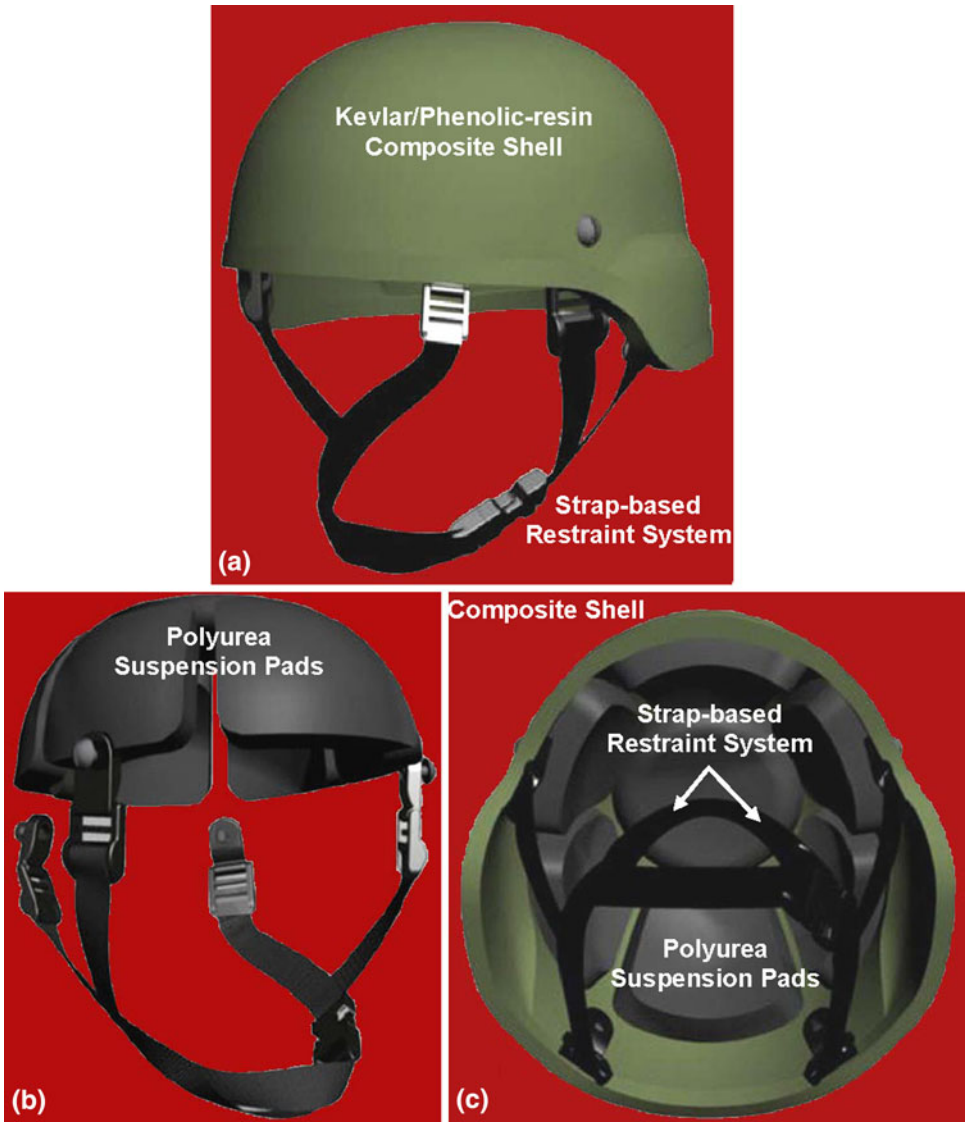

Fig. 1 The advanced combat helmet (ACH): (a) external side view, (b) suspension system side view, and (c) suspension system bottom view

The present work attempts to improve the understanding of the major phenomena and processes associated with the interaction of an air-borne blast wave with an ACH helmet-protected head. Following our recent investigation (Ref 9), the suspension pads are taken to be made of polyurea (a segmented and thermoplastically linked elastomer). In recent years, there have been various reports regarding the ability of this material to disperse shock waves propagating through and/or to efficiently dissipate the energy associated with such waves (e.g., Ref 10-12).

Interactions of air-borne blast waves with the human skull, subsequent generation of shock waves, and their direct or indirect propagation through intracranial soft tissue are very complex phenomena which are associated with a great deal of stochastic uncertainty. The two main causes of this uncertainty are: (a) explosive detonation is a very complex phenomenon and the waveform and intensity of the resulting blast wave and its associated three-dimensional pressure, density, velocity, and temperature hydrodynamic fields are greatly affected by the shape of the explosive, its chemistry, and its mode of detonation as well as by the characteristics of the surrounding ambient (air) and (b) direct interaction of blast waves with solid biological tissue leads to their reflection. It is well established that the subsequent interactions of the reflected blast waves with the soft tissue can result in shock waves whose intensity is increased multi-fold relative to that created by the primary blast waves (Ref 13, 14).

The main objective of the present work is to assess the ability of the ACH helmet, equipped with polyurea suspension pads, to mitigate the effect of shock waves generated during interaction of an air-borne blast wave with a helmet/head assembly. Following Moore et al. (Ref 15), two air-blast wave cases were considered in the present work: (a) the case associated with a peak overpressure of 5.2 atm corresponds to a blast-induced lung-injury threshold and is equivalent to a free-air explosion of 0.0698 kg of TNT at a standoff distance of 0.6 m and (b) an air-blast wave characterized by an 18.6 atm peak overpressure which corresponds to the 50% lethal dose (LD_{50}) for lung-injury related death and is equivalent to a free-air explosion of 0.324 kg of TNT at a standoff distance of 0.6 m.

Traditionally, the development of advanced blast and ballistic protection systems is carried out almost entirely using legacy knowledge and extensive fabrication/testing trial-and-error approaches. This approach is not only economically unattractive, but is often associated with significantly longer lead times. Consequently, this purely empirical approach has gradually become complemented by the appropriate cost- and time-efficient computer-aided engineering analyses. This trend has been accelerated by the recent developments in the numerical modeling of transient nonlinear dynamics phenomena such as those accompanying blast and ballistic loading conditions. In particular, recent advances have enabled the coupling between Eulerian solvers (used to model gaseous detonation products and air) and Lagrangian solvers [used to represent solid components of the protection systems, as well as of the projectiles (Ref 16)]. In the present manuscript, the coupled Eulerian-Lagrangian computational procedure used in our prior work (Ref 16) to analyze the occurrence of blast-induced TBI in the case of an unprotected human head is extended to the case of the head protected by a helmet containing polyurea suspension pads.

The organization of the article is as follows. A brief description of a typical transient nonlinear dynamics problem such as the one dealing with the interactions of an air-borne blast wave with the human head protected by a helmet is given in Section 2.1. Detailed descriptions of the geometrical and meshed models for the air/helmet/head assembly are presented in Section 2.2. A fairly detailed account of the material models assigned to air and the different sections of the helmet/head assembly is provided in Section 2.3. Formulation of the problem dealing with the interactions of an air-borne blast wave with the helmet/head assembly is presented in Section 2.4. The results obtained in the present work are presented and discussed in Section 3. The main conclusions resulting from the present work are summarized in Section 4.

2. Modeling and Computational Procedure

2.1 Transient NonLinear Dynamics Analysis of the Helmet/Head Assembly Subjected to Air-Borne Blast Waves

A typical transient nonlinear dynamics problem such as the interactions between an air-borne blast wave and a human head protected by a helmet involves solving simultaneously the governing partial differential equations for the conservation of momentum, mass, and energy along with the material constitutive equations and the equations defining the initial and the boundary conditions. The aforementioned equations are typically cast within a coupled Eulerian/Lagrangian formulation and solved numerically using a second order accurate explicit scheme, i.e., due to the large motions and deformations experienced by air, it is more computationally efficient to analyze the air region using an Euler control-volume computational scheme (the computational grid is fixed in space and time while the air moves through it). On the other hand, the helmet/head assembly which undergoes considerably less motion and deformation is analyzed using a Lagrange scheme (the computational grid is tied to the materials constituting the helmet/head assembly and moves and deforms with it).

All the calculations carried out in this work were done using ABAQUS/Explicit, a general purpose transient nonlinear dynamics analysis software (Ref 17). The interactions (including self-interactions) or bonding between different components of the model are analyzed using the appropriate Lagrange-Lagrange and Euler-Lagrange contact/sliding and kinematic coupling options. For example, Lagrange-Lagrange interactions are analyzed in ABAQUS/Explicit using a "penalty" contact method within which the penetration of the surfaces into each other is resisted by linear spring forces/contact pressures with values proportional to the depth of penetration. These forces, hence, tend to pull the surfaces into an equilibrium position with no penetration. Contact pressures between two Lagrangian bodies are not transmitted unless the nodes on the "slave surface" of one body contact the "master surface" of the other body. There is no limit to the magnitude of the contact pressure that could be transmitted when the surfaces are in contact. Transmission of shear stresses across the contact interfaces is defined in terms of a static and a kinematic friction coefficient as well as an upper-bound shear stress limit (a maximum value of shear stress which can be transmitted before the contacting surfaces begin to slide).

Interactions between an Eulerian region (containing air and a propagating blast wave) and a Lagrangian region (containing the helmet/head assembly) are treated as a fluid/solid interaction problem. In these types of problems, the Lagrangian-type solid

structures' free surfaces define the inner/contact boundaries for the Eulerian region (i.e., the Lagrangian region resides fully or partially within the Eulerian region and provides "no-flow" boundary conditions to the fluid in the direction of the local surface normal) while the Eulerian region provides pressure-loading boundary conditions to the Lagrangian region.

2.2 Geometrical and Meshed Models

Two distinct geometrical/mesh models are used in the present work: (a) a simple cube-shaped Eulerian-domain model was used to represent the ambient air and a single planar blast wave traveling through it and (b) a Lagrangian-domain model for the complete helmet/head assembly placed within the Eulerian domain. The two models are described in greater detail below.

2.2.1 Eulerian Domain. This cube-shaped domain with an edge length of 400 mm was meshed using eight-node cubic elements with an average edge length of 7 mm. Thus, the domain contains approximately 185,000 elements/cells, not including those elements occupied by the Lagrangian helmet/head assembly. Due to the Eulerian nature of the domain, the cells are not distorted/deformed during the analysis of blast-wave/helmet/head assembly interactions. However, in order to capture the hydrodynamic fields in the regions adjacent to the blast-wave front with higher resolution, an adaptive meshing algorithm was used which effectively attaches the mesh to the advancing blast wave. The Eulerian domain is filled with air. Details regarding the material model for air are presented in the next section.

2.2.2 Lagrangian Domain. The CAD model of the head developed in our previous work (Ref 16) was combined with the ACH helmet CAD model developed by www.turbosquid.com and meshed/preprocessed for the ABAQUS/Explicit finite-element program (Ref 17) using the general purpose pre-processing program HyperMesh from Altair, Inc. (Ref 18). The head model includes the following six sections: main brain (*cerebrum*), cerebrospinal fluid (CSF, *liquor cerebrospinalis*), small brain (*cerebellum*), brain stem (*truncus encephali*), pituitary gland (*glandula pituitaria*), and the skull (*cranium*) while the helmet model consists of an outer composite shell, seven suspension pads and a restraint system. These head components are identified in Fig. 2 while the helmet components are displayed in Fig. 1. In Fig. 3(a, b), both the cube-shaped Eulerian (transparent) and the Lagrangian domains are displayed for the cases of an unprotected head and a helmet-protected head, respectively. It should be pointed out that the standard bioengineering coordinate system was used in the present work (i.e., the finite-element model of the skull/brain assembly is oriented in such a way that the positive x-axis is pointing forward, y-axis upward, and z-axis from left to right).

The finite-element model of the helmet/head assembly (with 240 mm by 265 mm by 245 mm overall maximum dimensions along the three coordinate axes) used in the present work consists of approximately 550,000 first-order tetrahedral solid finite elements with a typical element edge length of 3 mm.

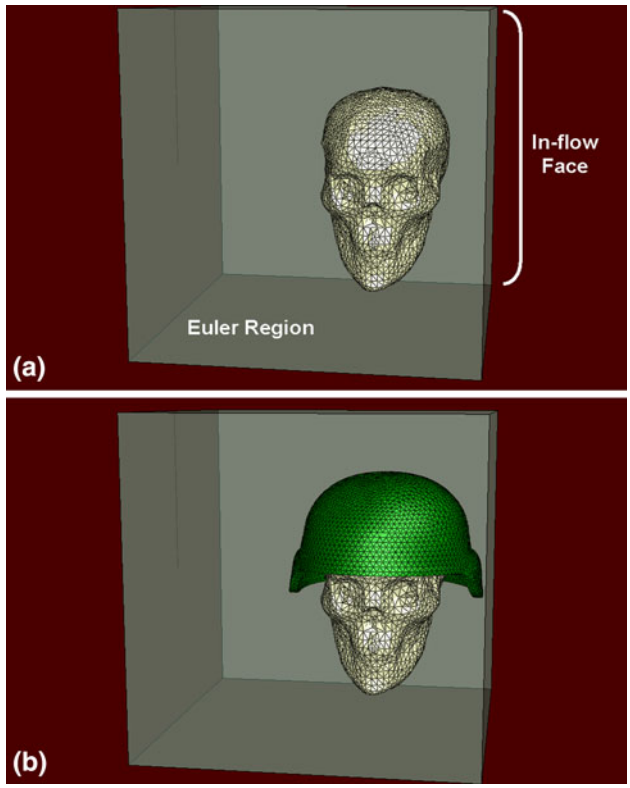

Fig. 3 The Eulerian/Lagrangian domain assembly used for the cases of: (a) an unprotected head and (b) a helmet-protected head

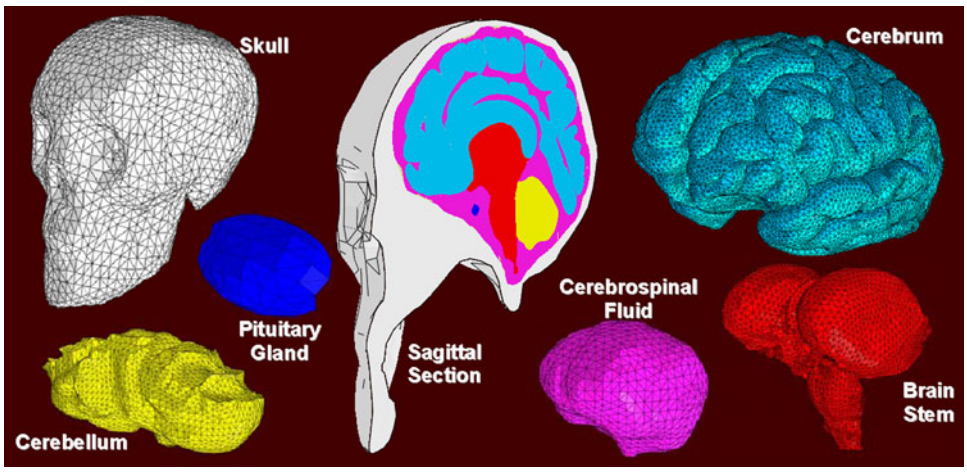

Fig. 2 Sagittal section of the human-head model and finite-element meshes of the skull and various brain sections

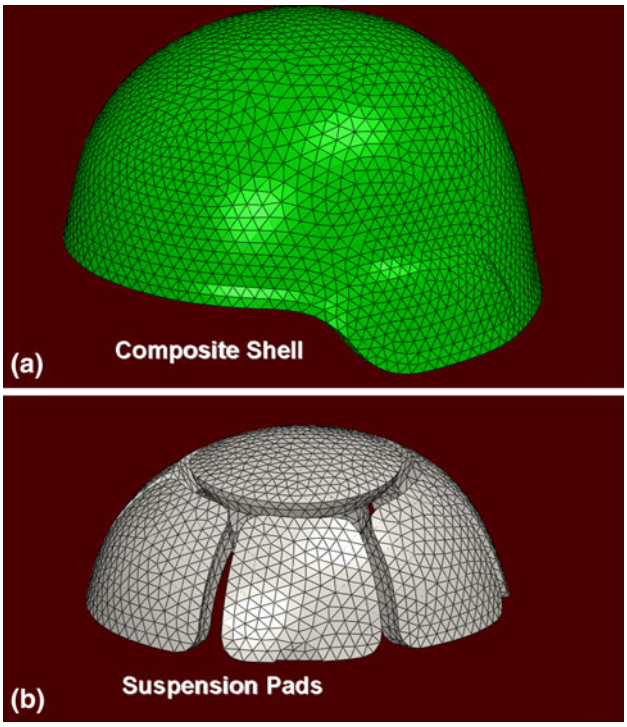

Fig. 4 The finite-element meshes of the ACH: (a) external composite shell and (b) elastomeric suspension pads

This Lagrangian mesh size was found to be a good compromise between accuracy and computational efficiency. The use of finer meshes was found to produce somewhat different numerical values of the key field quantities. However, they did not alter the nature of the basic findings obtained in the present work. Typical head and helmet finite element meshes used in the present work are displayed in Fig. 2 and 4, respectively. Connections between adjacent head sections were established by having them share nodes along adjoining interfaces while contact surfaces are created between the suspension pads and the skull/composite shell.

The next section identifies the materials used in the helmet/head assembly as well as in the surrounding ambient atmosphere and presents their constitutive models suitable for use under blast-induced high deformation rate conditions.

2.3 Material Models

The complete definition of a transient nonlinear dynamics problem (such as the interactions of blast waves with the helmet) entails the knowledge of the material models that define the relationships between the flow variables (pressure, mass-density, energy-density, temperature, etc.). These relations typically involve an equation of state, a strength model, and a failure model for each constituent material. These equations arise from the fact that, in general, the total stress tensor can be decomposed into a sum of a hydrostatic stress (pressure) tensor (which causes a change in the volume/density of the material) and a deviatoric stress tensor (which is responsible for the shape change of the material). An equation of state is then used to define the corresponding functional relationship between pressure, mass-density, and internal-energy density/temperature, while a strength model is used to define the appropriate relations between the deviatoric part of the stress tensor and various quantities characterizing the extent and rate of material deformation as well as the effect of material temperature. In addition, a material model generally includes a failure model, i.e., an equation describing the (hydrostatic or deviatoric) stress and/or strain condition(s) which, when attained, causes the material to fracture and lose its ability to support tensile normal and shear stresses. Due to the fact that blast levels considered in the present work typically do not cause any detectable damage to the helmet, skull or the inter-cranial brain matter and due to the fluid nature of air, failure of the materials encountered in the present problem was not considered. Likewise, since blast loading scenarios considered in the present work are not generally accompanied with significant thermal radiation or heat generation via energy dissipation, the effect of temperature on the material behavior was not considered.

As mentioned earlier, the present work investigates interactions between an air-borne blast wave and the helmet/head assembly. Since these interactions typically result in the formation of shock waves within the helmet/head assembly, special attention was paid to the ability of the material models used in the present work to enable formation of the shock waves. Specifically, as discussed in our prior work (Ref 16), formation of shock waves demands that the associated pressure versus specific volume (reciprocal of the density) relationship be nonlinear and concave upward (i.e., pressure increases at a higher and higher rate as the specific volume decreases).

2.3.1 Air Material Model. As mentioned earlier, the Eulerian domain was filled with air. Air was modeled as an ideal gas and, consequently, its equation of state was defined by the ideal-gas gamma-law relation as (Ref 19):

$$P = (\gamma - 1)\frac{\rho}{\rho_0}E, \qquad \text{(Eq 1)}$$

where P is the pressure, γ is the constant-pressure to constant-volume specific heat ratio (=1.4 for a diatomic gas like air), ρ_0 (=1.225 kg/m^3) is the initial air mass density, and ρ is the current mass density. For Eq (1) to yield the standard atmospheric pressure of 101.3 kPa, the (initial) internal volumetric energy density E was set to 261.2 kJ/m^3 which corresponds to the air mass specific heat of 717.6 J/kg per K and a reference temperature of 298 K. Since according to Eq (1), P scales linearly with ρ (i.e., with the reciprocal of the specific volume), the present model enables shock formation.

Since air is a gaseous material, it has no ability to support shear stresses and no strength model was defined for this material.

2.3.2 Kevlar/Phenolic-Resin Composite Material Model. Following the work presented in Ref 20, Kevlar/Phenolic-resin composite material has been modeled using an orthotropic equation of state and an orthotropic linear-elastic strength model. Within the orthotropic equation of state, pressure is defined as:

$$\begin{aligned} P = &- K_1 e_{\text{vol}} + K_2 e_{\text{vol}}^2 - \frac{1}{3}(C_{11} + C_{21} + C_{31})e_{11}^{\text{d}} \\ &- \frac{1}{3}(C_{12} + C_{22} + C_{32})e_{22}^{\text{d}} \\ &- \frac{1}{3}(C_{13} + C_{23} + C_{33})e_{33}^{\text{d}}, \end{aligned} \qquad \text{(Eq 2)}$$

where $K_1 = \frac{1}{9}(C_{11} + C_{22} + C_{33} + 2(C_{12} + C_{23} + C_{31}))$ is the effective bulk modulus, e_{vol} is the volumetric strain, K_2 is a nonlinear correction to the P versus e_{vol} (=density) and the last three terms on the right-hand side of Eq (2) represent the contributions of the deviatoric strains, e_{ij}^{d}, to the pressure.

These contributions are absent in the case of an isotropic linear-elastic material. It should be noted that the presence of the $K_2\epsilon_{vol}^2$ term in Eq (2) introduces the material volumetric nonlinearity which is required for the formation of shock waves.

The Kevlar/Phenolic-resin composite strength model is simply defined by a generalized Hooke's law which uses the elastic stiffness matrix to map the deviatoric strain components to the corresponding deviatoric stress components. The components of the elastic stiffness matrix, C_{ij}, appearing in Eq (2) and in the equation for K_1, are defined in terms of the corresponding engineering constants E_{ii}, G_{ij}, and ν_{ij} (i,j = 1,2,3) using standard relations. A summary of the Kevlar/Phenolic-resin composite material model parameters can be found in our previous work (Ref 9).

2.3.3 Polyurea Material Model. The mechanical response of polyurea under blast loading conditions is represented using the material model reported in Ref 21. Within this model, the hydrostatic response of the material is considered to be elastic while the deviatoric response of the material is assumed to be time dependent and hence treated using a geometrically nonlinear visco-elastic formulation.

Within the hydrostatic part of the model, pressure is defined as:

$$P = -K(T)\frac{\ln(J)}{J}; \quad K(T) = K(T_{ref}) + m(T - T_{ref}), \qquad \text{(Eq 3)}$$

where subscript ref is used to denote a quantity at the reference temperature, K is the bulk modulus, T is the temperature, m is a material parameter, and J (=det(F)) with F being a quantity which maps the original/reference material configuration into the current/deformed material configuration. Since ln(J) represents the volumetric strain, the effective bulk modulus $K(T)/J$ increases with an increase in volumetric compression thus enabling formation of shock waves.

To account for the aforementioned time-dependent character of the deviatoric material response, evaluation of the deviatoric stress, σ', at the current time t has to be taken into consideration the entire deformation history of a given material point from the onset of loading at $t = 0$ to the current time. Based on the procedure outlined in Ref 21, σ' is defined as:

$$\sigma'(t) = 2G_\infty \frac{T}{T_{ref}} \int_0^t \left(1 + \sum_{i=1}^{n} p_i \exp\left(\frac{-(\xi(t) - \xi(\tau))}{q_i}\right) D'(\tau)\right) d\tau, \qquad \text{(Eq 4)}$$

where G_∞ is the "long-term" shear modulus (i.e., the value of the shear modulus after infinitely long relaxation time), n is the number of terms in the Prony series exponential-type relaxation function, p_i and q_i are, respectively, the strength and the relaxation time of each Prony series term, ξ is the so-called reduced time and D' is the deviatoric part of the rate of deformation tensor, D ($D'_{ij} = D_{ij} - 1/3 * D_{ii}\delta_{ij}$, i,j = 1,2,3, δ_{ij} is the Kronecker delta second-order tensor and summation is implied over the repeated indices). The reduced time concept is used to take into account the effect of temperature and pressure on the relaxation kinetics and is defined as:

$$\xi(t) = \int_0^t \frac{dt}{10^{A(T - C_{TP}P - T_{ref})/(B + T - C_{TP}P - T_{ref})}}, \qquad \text{(Eq 5)}$$

where A, B, and C_{TP} are material constants. Thus, the effect of temperature, T, and pressure, P, over a time period t on the material response is assumed to be identical to the material response at the reference temperature and pressure over a time period $\xi(t)$. The rate of deformation tensor, D, is related to the deformation gradient, F, as:

$$D = \mathrm{sym}\left(\dot{F}F^{-1}\right), \qquad \text{(Eq 6)}$$

where "sym," the raised dot and superscript "−1," are used to denote, respectively, the symmetric part, the time derivative, and the inverse of a second-order tensor.

A summary of the polyurea material model parameters can be found in our previous work (Ref 9).

2.3.4 Skull Material Model. Skull is composed of bone material, which is characterized by relatively high levels of hydrostatic and deviatoric rigidity/stiffness. The hydrostatic part of the skull material model is represented using the Mie-Gruneisen equation of state of the form:

$$P = \frac{\rho_0 C_0^2 \left(1 - \frac{\rho_0}{\rho}\right)}{\left[1 - s\left(1 - \frac{\rho_0}{\rho}\right)\right]^2}, \qquad \text{(Eq 7)}$$

where ρ_0 is the initial/reference density and coefficient C_0 (the sound speed) and s relates the shock speed U_s and the resulting particle velocity, U_p, as:

$$U_s = C_0 + s \cdot U_p \qquad \text{(Eq 8)}$$

Equation (7) also referred to as a shock-Hugoniot equation of state, is often used to introduce material volumetric nonlinearities and, thus, to promote the formation of shocks in solid materials. The values for the equation of state parameters ρ_0, C_0, and s for the skull material can be found in our previous work (Ref 9).

Due to the high shear rigidity of skull material and resulting small shear strains, the deviatoric response of this material is defined as linear elastic. Consequently, this response is quantified by a single material parameter, the shear modulus μ, defined in terms of the corresponding Young's modulus E and the Poisson's ratio ν, as $\mu = E/2(1 + \nu)$. The E and ν values for the skull material can be found in our previous work (Ref 9).

2.3.5 Brain-Tissue Material Models. It is well-recognized that due to the interplay between a number of phenomena such as nonlinear visco-elasticity, anisotropy, extreme rate dependency/sensitivity, etc., the behavior of brain-tissue materials is highly complex. In addition, the consistency and constituent response of soft biological tissues is generally associated with considerable variability. Consequently, following the analyses carried out in our prior work (Ref 16), simpler material models which rely on relatively few parameters that can be determined with a greater statistical confidence were selected for use in the present work. Specifically, the materials constituting the cerebro-spinal fluid and cerebrum are assumed to be isotropic (direction-invariant), homogeneous (spatially uniform), elastic (time-invariant, materially nonlinear) materials with respect to their hydrostatic/volumetric response and as isotropic, homogeneous, visco-elastic or visco-hyper-elastic (time dependent, geometrically/materially nonlinear) with respect to their deviatoric/shear response.

In accordance with these observations/assumptions, the hydrostatic portion of the soft-tissue material model is defined

using an initial value of the bulk modulus and one or more parameters defining the type and extent of nonlinearity between the pressure, density, and internal energy.

Specifically, following Moore et al. (Ref 15), the nonlinear hydrostatic/volumetric (pressure, P versus density, ρ) elastic response of brain-tissue materials is modeled using a Tait-type equation of state of the form:

$$P = B\left[\left(\frac{\rho}{\rho_0}\right)^{\Gamma_0+1} - 1\right], \qquad \text{(Eq 9)}$$

where B and Γ_0 are material-specific parameters. The Tait equation of state is commonly used to model the behavior of fluids under high pressures (including the formation of shocks) and, due to the chemical similarity between brain tissue and water as well as the attendant blast-induced high pressures, was deemed an appropriate choice. Due to the aforementioned similarity between water and the brain tissue, Γ_0 was set to its value of 6.15 in water while B was determined from the condition:

$$K = B \cdot (\Gamma_0 + 1), \qquad \text{(Eq 10)}$$

where K is the (initial) bulk modulus. A summary of the Tait equation of state parameters ρ_0, B, and Γ_0 for the brain-tissue materials can be found in our previous work (Ref 16).

The deviatoric/strength part of the material model was initially considered to be visco-elastic and to include a time-dependent shear modulus (diminishing from an initial larger value to a smaller long-term value) as well as one or more parameters accounting for the type and extent of geometrical/material nonlinearities. It was soon recognized that the shear modulus relaxation times for the intra-cranial materials in question are on the order of tens or hundreds of milliseconds and are, thus, several orders of magnitude larger than the characteristic blast-wave/human-head interaction times. Under these conditions, it was deemed justified to assume that time-dependent shear-deformation effects play a secondary role in the response of the brain materials to the blast. Therefore, the deviatoric portion of the material response was assumed as time-invariant. However, a provision had to be made for the potential effect of large-deformation induced geometrical and material nonlinearities and, consequently, the deviatoric portion of the material model was defined using a hyper-elastic formulation. Following the analysis carried out in our prior work (Ref 16), a Neo-Hookean hyper-elastic model was selected which defines the deviatoric stress as:

$$\sigma' = J^{-1}F\left[\mu \cdot \left(\log\sqrt{C}\right)^{\text{dev}}\right]F^{\text{T}}, \qquad \text{(Eq 11)}$$

where F and J were defined previously, μ is the shear modulus and $C = F^{\text{T}}F$ (is the right Cauchy-Green deformation tensor, and superscript T is used to denote a transpose). For simplicity, the $\sqrt{C}$ term is replaced with its first-order and second-order linearized forms (Ref 22). A summary of the Neo-Hookean hyper-elastic model parameters can be found in our previous work (Ref 16).

2.4 Problem Formulation

Interactions between an air-borne blast wave and an unprotected/protected head was analyzed in the following way: (a) the initial pressure in Eulerian domain is set to the atmospheric level; (b) an Eulerian "in-flow" face, which is parallel to the x-y plane and adjacent to the left-hand side of the helmet/head assembly (from the perspective of the blast subject), is defined to enable influx of air material associated with the blast wave wake. A time-dependent pressure impulse is next prescribed over this face in accordance with the bi-phasic Friendlander pressure versus time function, Fig. 5. Parameter identification for this function was carried out using the blast simulation code, ConWep, developed by the US Army Corps of Engineers (Ref 23). As mentioned earlier, two air-blast wave cases were considered in the present work: (a) the case associated with a peak overpressure of 5.2 atm and (b) an air-blast wave characterized by an 18.6 atm peak overpressure. As a result of the time-varying pressure application over the in-flow face, a blast wave enters the Eulerian domain and propagates toward the air/helmet contact surface. On reflection of the blast wave from this contact surface, the reflected wave propagates in the opposite direction and ultimately exits the Eulerian domain; (c) "Out-flow" boundary conditions are applied over the Eulerian-domain face parallel with the in-flow face; and (d) sliding "no-flow" boundary conditions were applied over the remaining Eulerian domain faces.

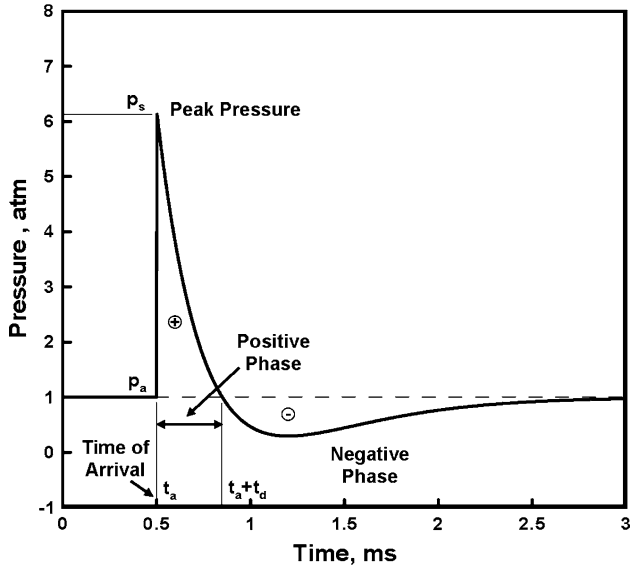

Fig. 5 A typical free-air pressure vs. time relation at a fixed point as defined by the biphasic Friendlander equation

As far as the boundary conditions are concerned, the following two types were applied simultaneously: (a) to mimic the skull/spine pivot joint; a coupling is created using a set of nodes at the skull base and the associated reference node is kinematically constrained to form a revolute joint and (b) to mimic the effect of neck-support muscles; six axial-type connectors are placed between four couplings on the skull and the base of the neck (modeled as a set of four nodes fixed in space). Using the approach outlined in our prior work (Ref 24), muscles are modeled as passive elastic elements and their elastic stiffness is set accordingly.

3. Results and Discussion

In this section and its subsections, the main results obtained in the present work are presented and discussed. It should be recalled that the standard bioengineering type of the global

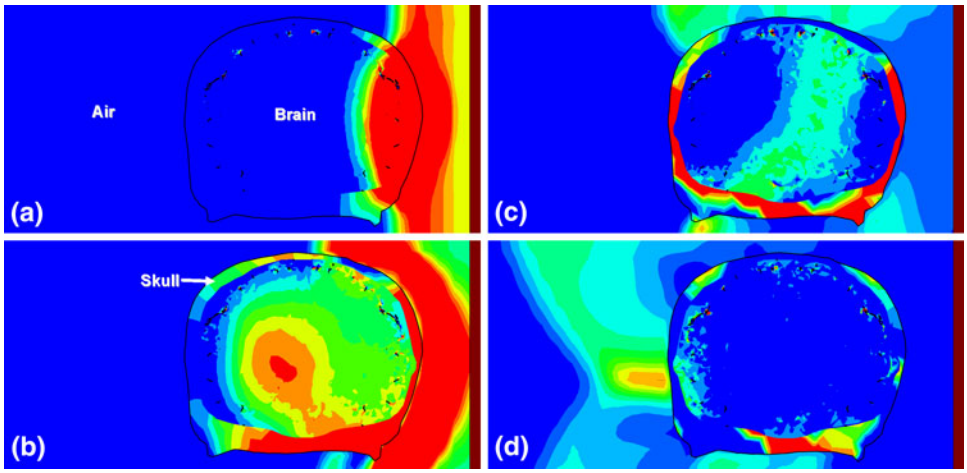

Fig. 6 An example of the temporal evolution of the pressure and its spatial distribution over the mid-coronal section in both the (air) Eulerian and the (skull/brain) Lagrangian domains

coordinate system was used in the present work. Within this coordinate system, the coronal section of the brain is parallel with the *y*-*z* plane, while the sagittal section is parallel with the *x*-*y* plane. These sections will be used for displaying the spatial distribution and temporal evolution of some of the hydrodynamic field quantities. In accordance with the radiological convention, only blast impact over the right (from the perspective of an observer facing the blast subject) temporal region of the skull was considered.

An example of the temporal evolution of the pressure and its spatial distribution over the mid-coronal section in both the Eulerian and the Lagrangian domains for the case of an unprotected head is displayed in Fig. 6(a-d). It is seen that the air-borne blast wave propagates from the right side and, on impacting the skull, produces a shock pressure wave at the impacted head side. As expected, the shock pressure wave is seen to travel at a higher speed through the intra-cranial matter than the blast wave does through the air. Consequently, by the time the air-borne blast wave reaches the left-hand side of the skull, the shock wave within the intra-cranial cavity has undergone several reflections from the brain/skull and skull/air interfaces. Also, it can be observed that, as the shock wave propagates through the brain and undergoes multiple reflections, it undergoes attenuation and dispersion/decomposition. Qualitatively similar results were obtained in the helmet-protected head case (the results not shown for brevity) although the pressure levels within the intra-cranial cavity are found to be substantially lower.

Since the present work involves blast impact simulations for the unprotected and the helmet-protected head cases and for each the analysis was done at two different blast peak pressures, the results in the remainder of this section will be presented accordingly.

3.1 Unprotected-Head Case

3.1.1 5.2 atm Peak-Pressure Blast Impact. The first challenge that had to be overcome was the selection of the field quantities which are relevant to (i.e., play a critical role in the occurrence of) TBI. Toward that end, the following three most common types of non-penetrating TBI are first identified: (a) diffuse axonal injury, (b) contusion, and (c) subdural hemorrhage (Ref 2).

Diffuse axonal injuries are believed to be caused by blast-induced stretching and shearing of axons and small vessels which, in turn, lead to impaired axonal transport and subsequent focal axonal swelling and eventual disconnection (Ref 2). The most common locations for this type of TBI are the cortico-medullary (gray matter-white matter) junction (particularly in the frontal and temporal areas), internal capsule, deep gray matter, upper brainstem, and the corpus callosum (Ref 2). To help the reader relate to the most probable locations of the three types of TBI, a surface-topology and a median sagittal-section brain map are provided in Fig. 7(a, b), respectively (Ref 25). In line with these observations, it was decided to monitor temporal evolution and spatial distribution of maximum principal (tensile) stress and maximum shear stress within the intra-cranial cavity.

Contusions occur when the brain undergoes a sufficiently large relative motion with respect to the skull resulting in brain/skull collision. This typically leads to bruising (as well as hemorrhage and edema) of the brain parenchyma (functional parts of the brain tissue). The most common locations in this type of TBI are the superficial gray matter of the inferior, lateral, and anterior aspects of the frontal and temporal lobes, with the occipital poles or cerebellum less often involved (Ref 2). It should be noted that due to the fact that the CSF (modeled as a Lagrangian part, in the present work) permanently prevents a direct brain/skull contact, an alternative measure for the probability of the contact had to be defined. Toward that end, six pairs of CSF nodes (one node at the CSF/skull interface and the other at the CSF/brain interface) were selected and their distance monitored during the simulation. The location of these node pairs (marked as a-f) is displayed in the center inset of Fig. 10. The relative reduction in the distance of the paired nodes is then used as a measure of the brain/skull impact probability.

Subdural hemorrhage occurs when the surface layers of the brain experience severe distortions due to the ingress of blast-wave-induced shear stresses resulting in tearing of the tributary surface veins which connect the brain surface and the dural venous sinus (a vein hub which returns blood and cerebrospinal fluid to the jugular vein). Due to the visco-elastic dissipative nature of the brain-tissue material, shear stresses and distortions are highest in the frontal and parietal brain surface regions

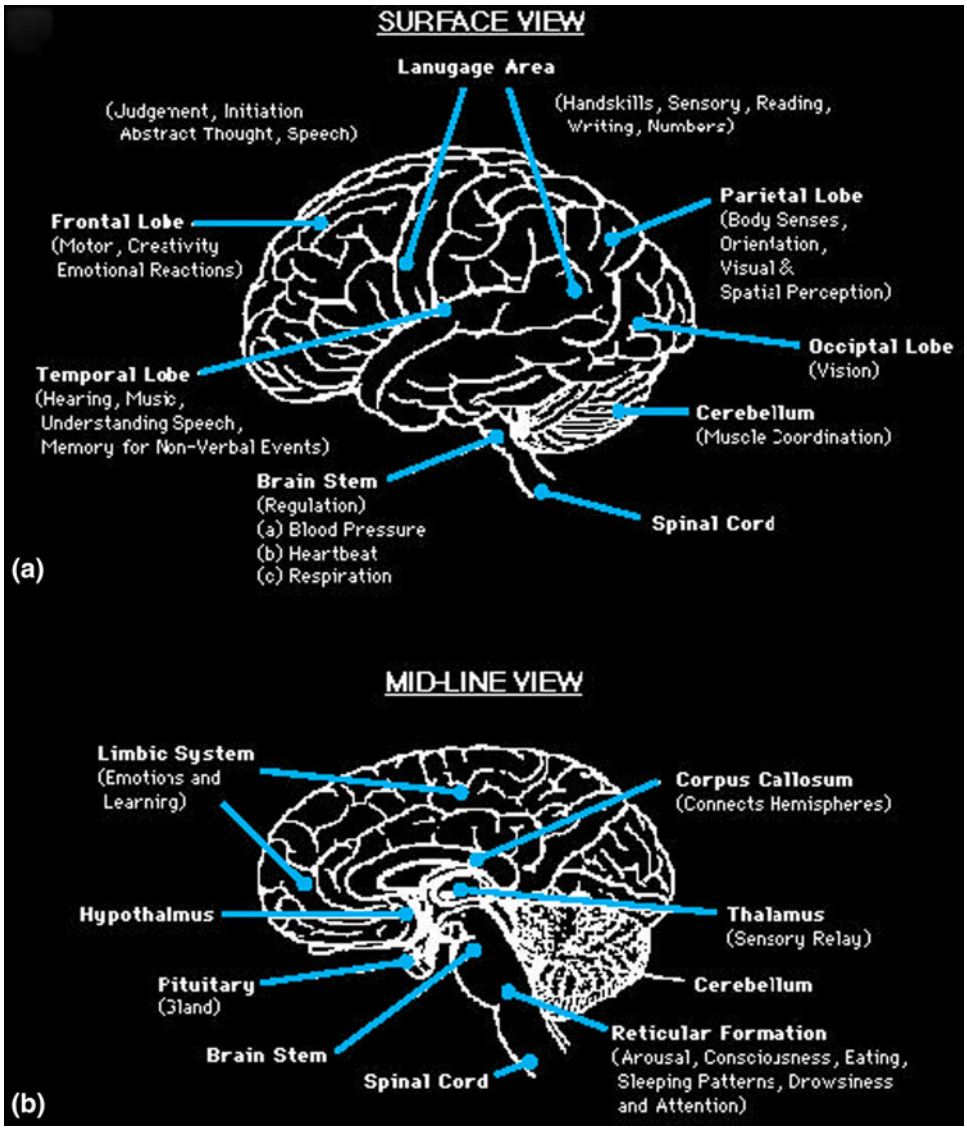

Fig. 7 A simple schematic of the brain map (Ref 25): (a) surface topology and (b) a median sagittal section

adjacent to the location of blast-wave ingress (Ref 2). In line with these observations, it was decided to monitor the spatial distribution of the peak values of the maximum shear stress over the surface of the brain lobes in order to identify conditions/locations with the potential for subdural hemorrhage occurrence.

Spatial distributions of the maximum principal normal stress over the mid-coronal ($x = 0$) section at four different post-blast times (0.11, 0.16, 0.21, and 0.29 m s), for the unprotected head/5.2 atm peak-pressure case are displayed in Fig. 8(a-d) (the term "post-blast time" is used in the present work to denote the simulation run-time, where $t = 0$ represents the time at which the blast-wave front is located at the Euler in-flow boundary). The corresponding maximum shear stress results are displayed in Fig. 9(a-d) at four different post-blast times (0.10, 0.23, 0.36, and 0.49 m s). As will be discussed later, the post-blast times selected correspond to particularly significant intra-cranial shock wave propagation/reflection events. The maximum principal (tensile) stress limits in Fig. 8(a-d) are 800 and 500 kPa, while those for the maximum shear stress in Fig. 9(a-d) are 0.0 and 0.30 kPa. It should be noted that the impacted right-hand side of the skull is located on the right-hand side in Fig. 8(a-d) and 9(a-d), as well as in the subsequent hydrodynamic-quantity field figures. As mentioned earlier, high tensile and shear stresses are believed to be responsible for axonal damage (Ref 2), while high surface shear stresses are thought to cause subdural hemorrhage. It should be noted that arrows are used in Fig. 8(a-d) and 9(a-d), as well as in the subsequent hydrodynamic-quantity field plots, to indicate the direction of motion of the strongest shock wave within the intra-cranial cavity. A brief examination of the results displayed in Fig. 8(a-d) and 9(a-d) reveals that:

(a) Initial distribution of the maximum principal (tensile) stress and the maximum shear stress is controlled by the shock-wave transfer from the ambient air to the skull and, in turn, to the intra-cranial matter. Subsequent evolution of these quantities, on the other hand, appears to be primarily controlled by the multiple, complex reflections and interactions of the intra-cranial shock wave(s);

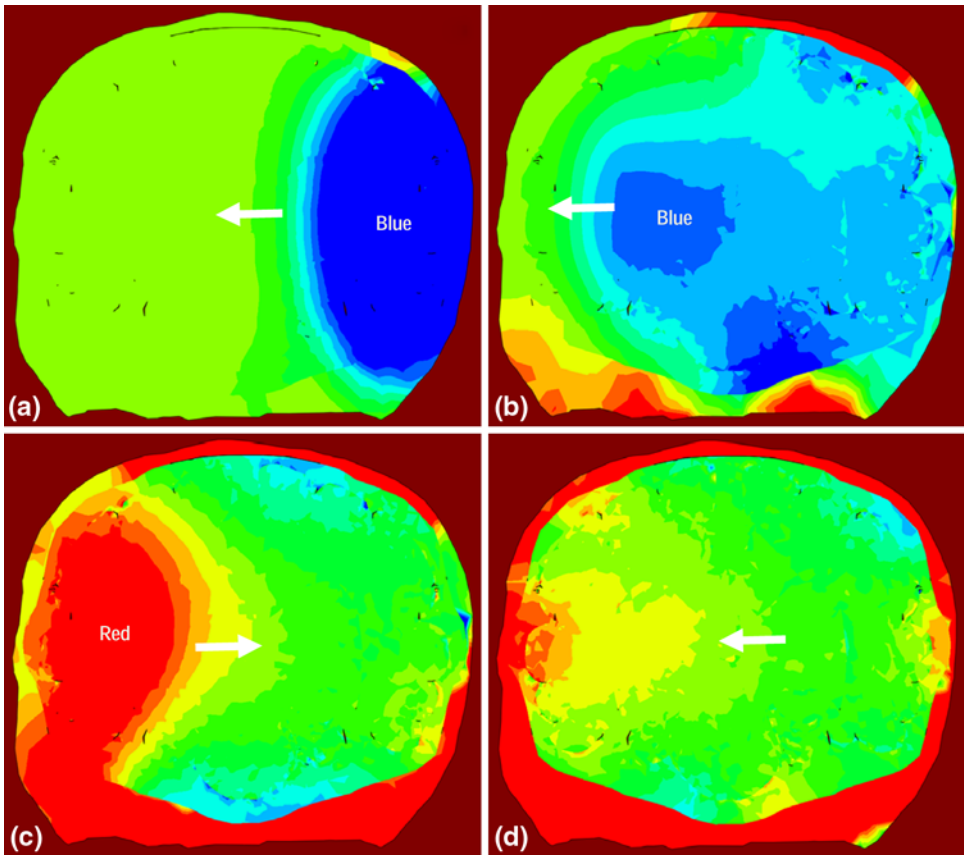

Fig. 8 Spatial distribution of the maximum principal stress over the mid-coronal section of the head, for the unprotected head case, at four post (5.2 atm peak pressure) blast impact times: (a) 0.11 m s, (b) 0.16 m s, (c) 0.21 m s, and (d) 0.29 m s. Maximum principal stress range: −800 kPa, 500 kPa

(b) The algebraically maximum principal (compressive) stresses (ca. −2.5 MPa) (denoted in the darkest shade of blue) in the brain are observed at the impacted side of the head at ca. 0.11 m s post-blast time, Fig. 8(a). It should be noted that the peak pressure in the air-borne blast wave was 5.2 atm, which is equal to 0.52 MPa. Hence, the interaction of the blast wave with the head has resulted in a roughly five-fold increase of the algebraically maximum principal (compressive) stresses;

(c) On the first reflection of the (compressive) shock wave from the brain/skull and skull/air interfaces (at the distal side of the head, i.e., on the side of the head opposite to the one impacted by the blast wave), tensile shock waves are generated. The maximum principal (tensile) stress associated with these waves is found to peak with a value of 1.0 MPa at a post-blast time of 0.21 m s [indicated by the red color in Fig. 8(c)];

(d) Soon after the first shock wave reflection (ca. 0.29 m s) significant tensile-normal shock wave dispersion/decomposition takes place. This finding is supported by the results in Fig. 8(d) which displays a fairly uniform intracranial tensile stress field;

(e) Intra-cranial shear-stress levels are substantially lower (ca. three orders of magnitude) than the principal stress levels, Fig. 9(a-d). This finding is consistent with the fact that the brain is fairly shear-compliant and that it is separated from the skull by a layer of nearly inviscid and highly shear-compliant CSF;

(f) In sharp contrast to the normal stresses, the shear stresses continue to build over the full simulation time;

(g) The peak values of the maximum shear stress are observed within the brain stem, Fig. 9(d), and this finding appears to be related to the fact that the brain-stem material possesses the highest shear stiffness among the intracranial materials; and

(h) The peak maximum shear stress never exceeds the 7.8 MPa threshold level as established by Zhang et al. (Ref 26, 27) for the case of the National Football League players' head-to-head collisions induced mTBI. Since the peak maximum shear stress levels observed in the case of the 5.2 atm blast impact are substantially below this mTBI threshold, it appears that under these blast impact conditions, the likelihood for mTBI is small-to-none.

Temporal evolutions of the CSF layer thickness at six locations are displayed in Fig. 10(a). As explained earlier, contusion-type TBI is caused by impact of the brain against the interior surface of the skull and, within the present work, local relative reductions in the CSF layer thickness are used as indirect measures of brain/skull impact probability. A brief examination of the results displayed in Fig. 10(a) reveals that the maximum value of the CSF layer relative-thickness reduction is ca. 0.003 and that it occurs at the Location A (impacted side of the head). Since this level of CSF thickness reduction is quite small, contusion-type TBI does

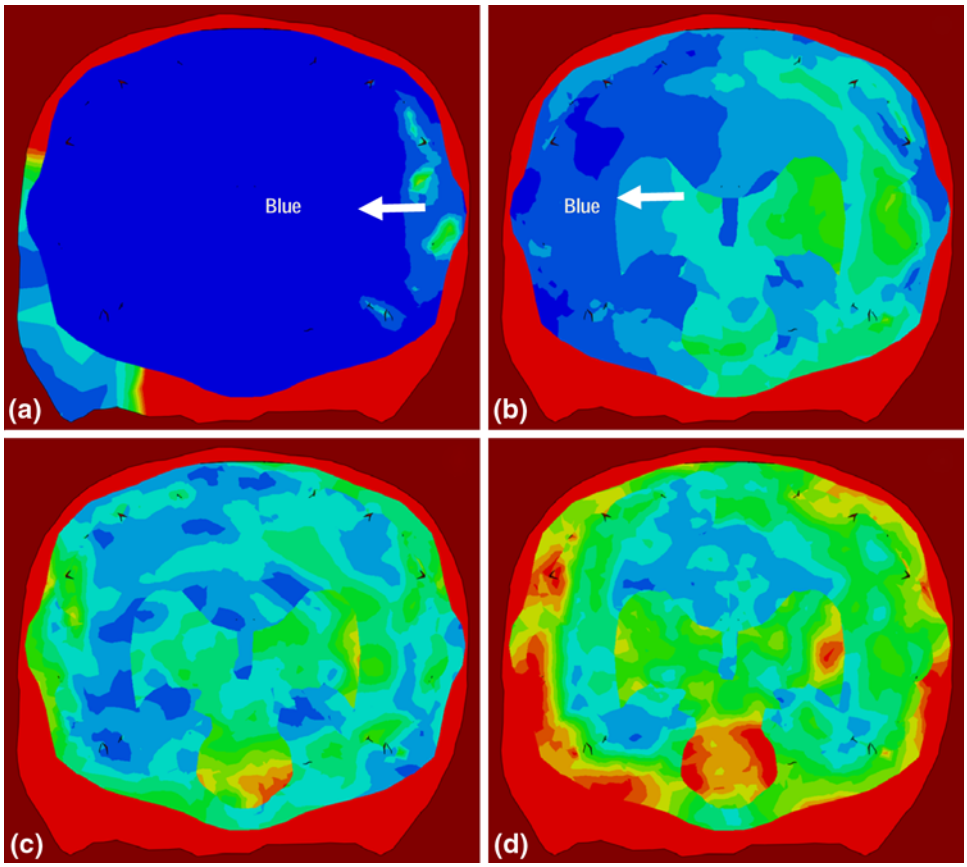

Fig. 9 Spatial distribution of the maximum shear stress over the mid-coronal section of the head, for the unprotected head case, at four post (5.2 atm peak pressure) blast impact times: (a) 0.10 m s, (b) 0.23 m s, (c) 0.36 m s, and (d) 0.49 m s. Shear stress range: 0.0 kPa, 0.3 kPa

not appear likely to occur in this case. However, one might exercise caution at this point since the results displayed in Fig. 10(a) indicate that CSF layer thickness reduction continues to take place with an increase in the simulation time in the distal part of the head (e.g., Location E). Hence, there is an increased likelihood of brain/skull collision at this location at post-blast time exceeding the current simulation times.

Spatial distribution of the maximum shear stress over the brain-lobe surfaces at a post-blast time (within the 1 m s simulation time used in the present work) at which this quantity experiences the largest value is displayed in Fig. 11(a). As explained earlier, subdural hemorrhage-type TBI is believed to be caused by large values of the surface shear stresses. The results displayed in Fig. 11(a) reveal that the peak value of the surface shear stress is 0.26 kPa and that the peak-stress location is in the distal temporal lobe. Since no surface shear stress threshold has been established for subdural hemorrhage-type TBI, one cannot use the peak values obtained to assess the likelihood of this type of TBI. However, relative values of the surface shear stresses at the two blast peak pressures and for the unprotected-head/protected-head cases will be compared in the remainder of Section 3 in order to assess the blast-mitigation efficacy of the ACH system.

3.1.2 18.6 atm Peak-Pressure Blast Impact. Spatial distributions and temporal evolutions of the maximum principal (tensile) stress and the maximum shear stress were also generated in this case. However, due to the space limitations and the fact that the results were qualitatively similar to their 5.2 atm counterparts, these results are not displayed here. The most important findings obtained by analyzing these results can be summarized as follows:

(a) On average, both maximum principal tensile stress and maximum shear stress are higher in the 18.6 atm case by a factor of 6-7, relative to the corresponding 5.2 atm quantities. This finding reiterates the previously mentioned nonlinear amplification of the blast wave on its collision with a solid structure; and
(b) As in the 5.2 atm blast peak-pressure case, the peak maximum shear stress never exceeds the mTBI-inducing 7.8 MPa threshold level.

Temporal evolution of the reduction of the CSF layer local thickness at the same locations as in the 5.2 atm case is displayed in Fig. 10(b). A comparison of the results displayed in Fig. 10(a, b) shows that an increase in the blast peak pressure from 5.2 to 18.6 atm (a ca. 257% increase) results in a 650-700% increase in the CSF-thickness reduction. At the same time, the place of the maximum reduction in CSF layer thickness has changed from Location A to Location E. In addition, it is seen that the CSF layer thickness reduction at Location E continues to increase with an increase in simulation time, suggesting that brain-skull collision probability will acquire higher values at post-blast times greater than the simulation times employed here.

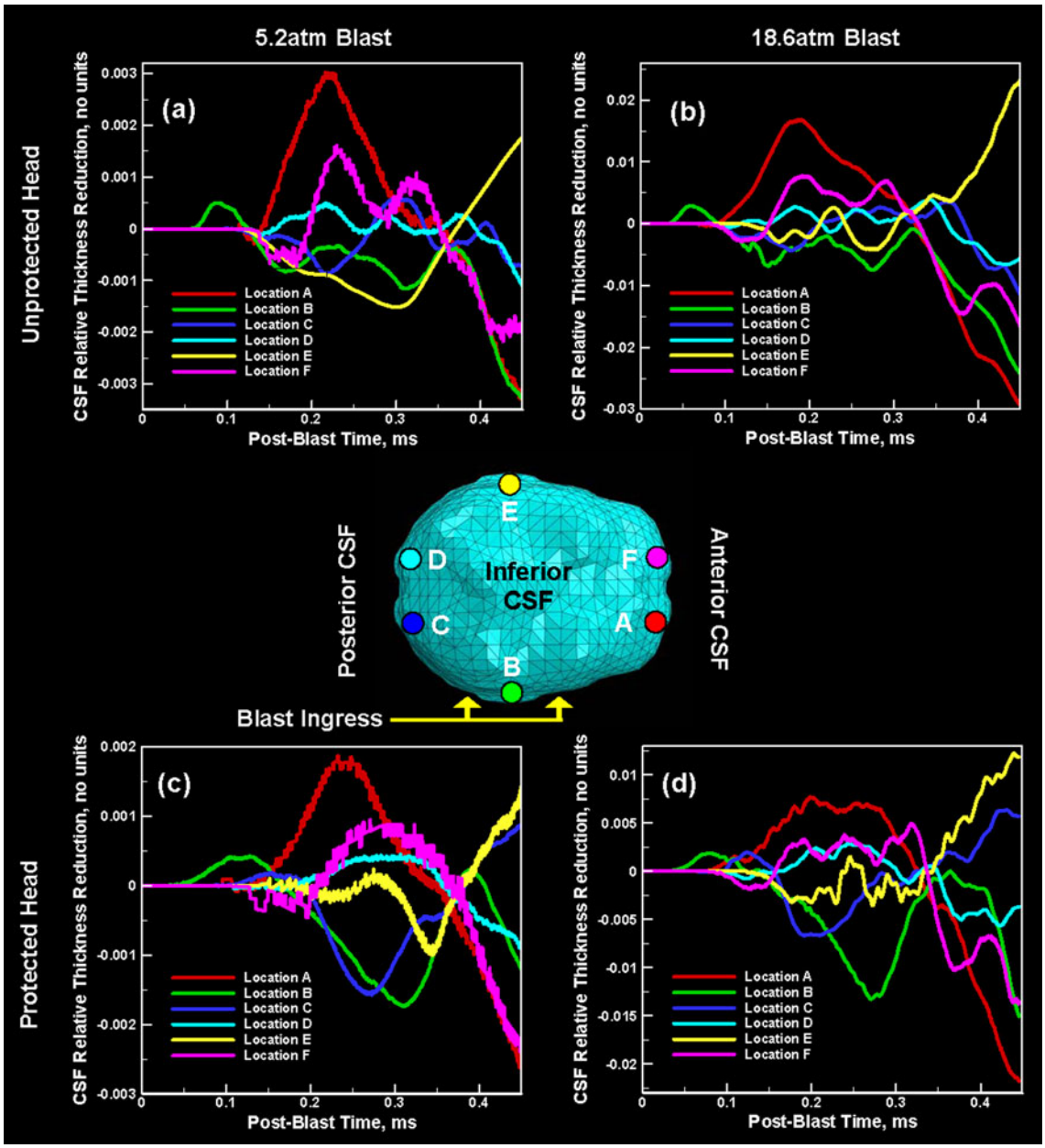

Fig. 10 The temporal evolution of the CSF local relative thickness change for the unprotected-head case (a) and (b), protected-head case (c) and (d), 5.2 atm peak pressures (a) and (c) and 18.6 atm peak pressure (b) and (d). Part (e) denotes the CSF locations monitored

The spatial distribution of the maximum shear stress over the brain-lobe surfaces at a post-blast time at which this quantity experiences the largest value is displayed in Fig. 11(b). A comparison of the results displayed in Fig. 11(a, b) shows that a ca. 257% increase in the blast pressure led to a 650% increase in the peak maximum surface-shear stress, while the most likely location of the subdural hemorrhage is seen to be at the proximal frontal lobe.

3.2 Helmet-Protected Head Case

3.2.1 5.2 atm Peak-Pressure Blast Impact. Spatial distributions of the maximum principal stress over the mid-coronal ($x = 0$) plane at four different post-blast times (0.13, 0.21, 0.30, and 0.38 m s) for the helmet-protected head/5.2 atm peak-pressure case are displayed in Fig. 12(a-d). The corresponding maximum shear stress results are displayed in Fig. 13(a-d) at four different post-blast times (0.10, 0.23, 0.36, and 0.49 m s). The maximum principal stress limits in Fig. 12(a-d) are −800 and 500 kPa while those for the maximum shear stress in Fig. 13(a-d) are 0.0 and 0.3 kPa. A brief examination of the results displayed in Fig. 12(a-d) and 13(a-d) reveals that:

(a) Initial distribution of the maximum principal (tensile) stress and the maximum shear is controlled by the shock-wave transfer from the ambient air to the ACH shell and then from the shell into the polyurea pads which directly load the skull. In this manner, the skull does not experience direct impact of the impinging blast wave as in the case of the unprotected head, but instead the skull is loaded through the helmet suspension pads

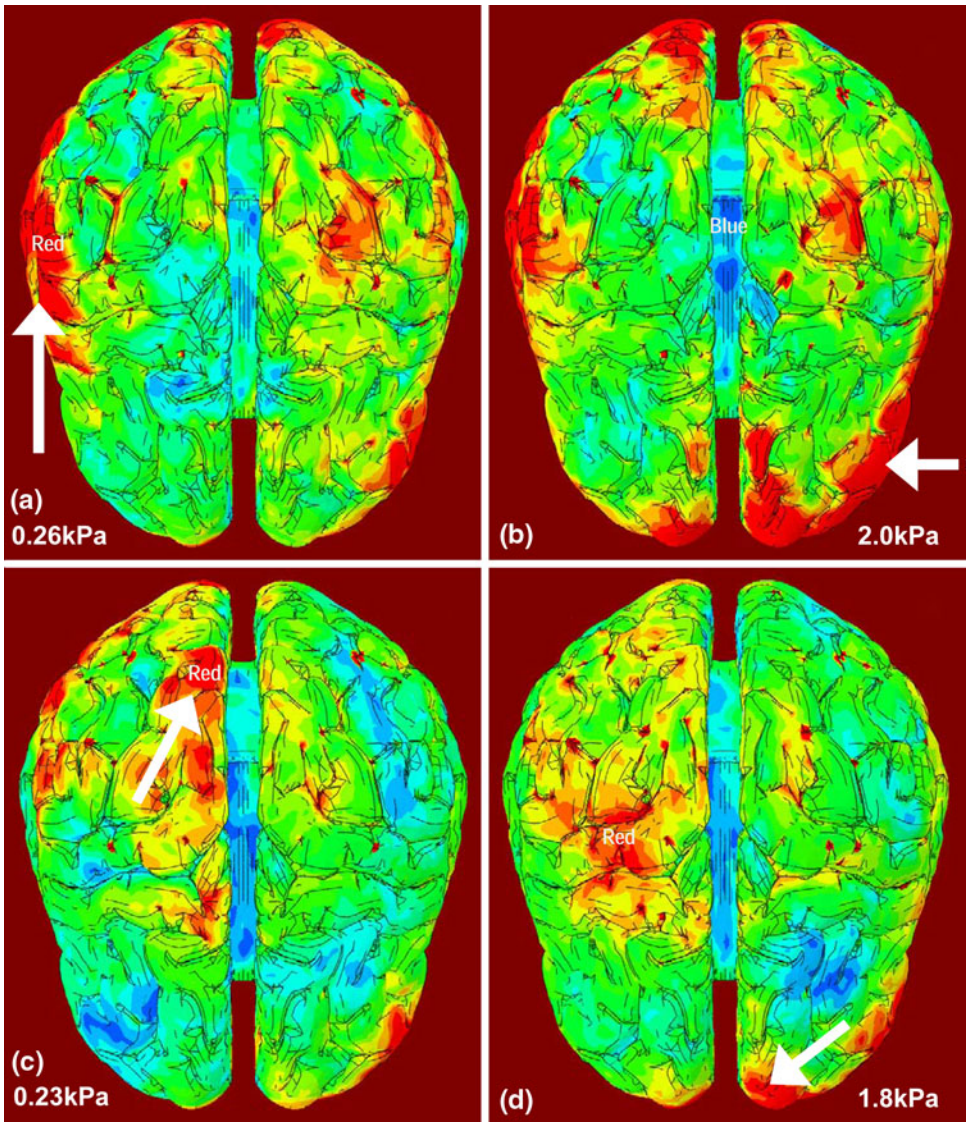

Fig. 11 Spatial distribution of the maximum shear stress over the surface of the brain-lobe at the instant when the stress reaches a maximum value for the unprotected-head case (a) and (b), protected-head case (c) and (d), 5.2 atm peak pressures (a) and (c) and 18.6 atm peak pressure (b) and (d). Note: 5.2 atm (0 kPa, 0.2 kPa), 18.6 (0 kPa, 1.3 kPa)

and through the blast "wash" pressure wave that enters from the helmet rim (Fig. 12b). This change in the intracranial loading path can be observed through comparison of Fig. 8(a) and 12(a). Subsequent evolution of the tensile/shear stresses, however, as in the case of the unprotected head, still appears to be primarily controlled by the multiple, complex reflections and interactions of the intra-cranial shock wave(s);

(b) The algebraically maximum principal (compressive) stresses (ca. −1.5 MPa) [denoted by the darkest blue color in Fig. 12(a)] in the intracranial region are observed directly below the skull-pad contact interface on the blast wave impacted side of the ACH/head at ca. 0.13 m s post-blast time, which represents a 1.0 MPa (40%) decrease in maximum principal stress magnitude and a 0.02 m s delay relative to the unprotected head case;

(c) On the first reflection of the (compressive) shock wave at the material interfaces (located at the distal side of the head), the maximum principal (tensile) stresses were observed adjacent to the skull/CSF interface with a value of 0.5 MPa [marked by the red shading in Fig. 12(c)] at a post-blast time of 0.30 m s. These stress levels are lower by approximately a factor of three relative to those observed in the corresponding unprotected-head case;

(d) Intra-cranial shear-stress levels are, again, substantially lower by ca. three orders of magnitude compared to the principal stress levels, Fig. 13(a-d). It is also observed that the maximum shear stresses continually build over the full simulation time in a similar manner to that of the intracranial shear stresses in the unprotected head case; and

(e) A comparison of the peak maximum shear stress over the coronal cut plane for the unprotected head case, Fig. 9(d), and helmet-protected head case, Fig. 13(d), reveals a 0.04 kPa (8%) decrease.

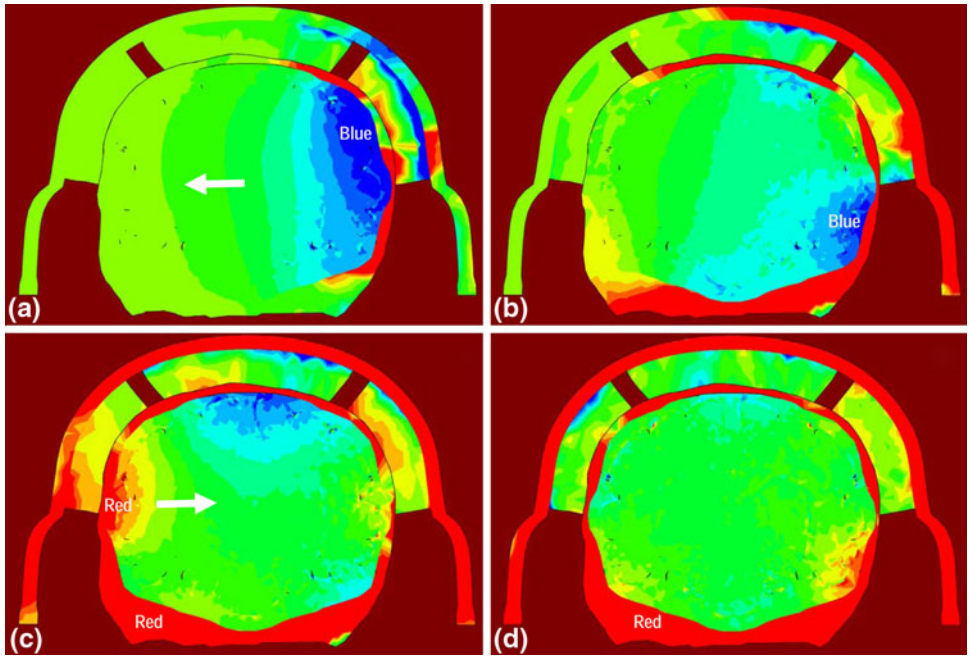

Fig. 12 Spatial distribution of the maximum principal stress over the mid-coronal section of the head, for the protected head case, at four post (5.2 atm peak pressure) blast impact times: (a) 0.13 m s, (b) 0.21 m s, (c) 0.30 m s, and (d) 0.38 m s. Maximum principal stress range: −800 kPa, 500 kPa

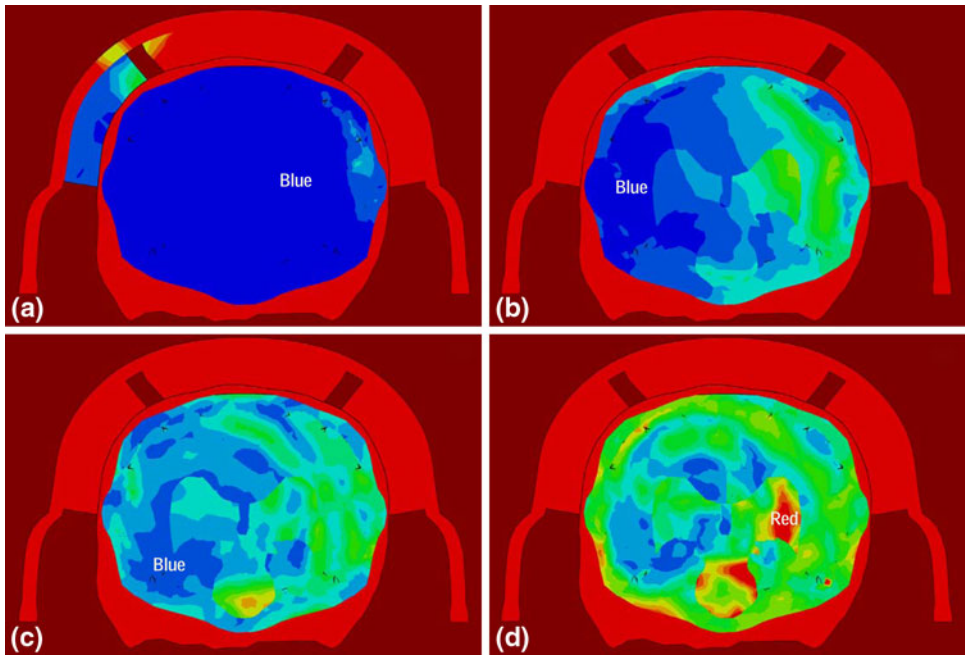

Fig. 13 Spatial distribution of the maximum shear stress over the mid-coronal section of the head, for the protected head case, at four post (5.2 atm peak pressure) blast impact times: (a) 0.10 m s, (b) 0.23 m s, (c) 0.36 m s, and (d) 0.49 m s. Shear stress range: 0.0 kPa, 0.3 kPa

Temporal evolution of the reduction of the CSF layer local thickness at the same locations as in the unprotected head case is displayed in Fig. 10(c). A comparison of the results displayed in Fig. 10(a, c) shows that the addition of an ACH helmet decreases the corresponding reduction in the CSF layer relative local thickness from 0.003 to 0.002 (a ca. 33% change) while the location associated with the highest brain/skull collision probability has not changed. Since this reflects a significant reduction in the brain/skull impact probability, the ACH appears to provide efficient protection against the blast-induced contusion-type TBI. However, it should be observed that, as in the unprotected-head case, the likelihood for brain/skull collision in the distal portion of the head continues to increase with the simulation time.

The spatial distribution of the maximum shear stress over the brain-lobe surfaces at a post-blast time at which this quantity experiences the largest value is displayed in Fig. 11(c). A comparison of the results displayed in Fig. 11(a, c) reveals that the addition of an ACH helmet decreases the peak value of the maximum surface-shear stress from 0.26 to 0.23 kPa (a 12% change), while the peak-stress location has moved only slightly.

3.2.2 18.6 atm Peak-Pressure Blast Impact. Spatial distributions and temporal evolutions of the maximum (tensile) principal stress and the maximum shear stress were also generated in this case. However, due to the space limitations and the fact that the results were qualitatively similar to their 5.2 atm counterparts, these results are not displayed here. The most important findings obtained by analyzing these results can be summarized as follows:

(a) On average, the maximum principal (tensile) stress and maximum shear stress are higher in the ACH head protected 18.6 atm case by a factor of ~5 and ~6, respectively, relative to the corresponding ACH head protected 5.2 atm quantities; and
(b) Relative to the unprotected head at the same 18.6 atm blast peak pressure, the maximum principal (tensile) stress was lower by 4.7 MPa (ca. 65%) and the shear stress was lower by 0.9 MPa (20%). These findings reveal that the ACH significantly lowers both the normal and shear peak-stress levels observed in the intracranial region and, thus, substantially reduces the likelihood for axonal damage-type TBI. It should be further noted that the ACH efficiency in lowering intracranial peak stresses is enhanced at higher levels of the blast peak pressure.

Temporal evolution of the reduction of the CSF layer local thickness at the same locations as in all previous cases is displayed in Fig. 10(d). A comparison of the results displayed in Fig. 10(c, d) shows that an increase in the blast peak pressure on a helmet-protected head from 5.2 to 18.6 atm (a ca. 257% increase) results in a 600-700% increase in the CSF-thickness reduction. In addition, a comparison of the results displayed in Fig. 10(b, d) reveals a nearly 50% lower CSF-thickness reduction while the location associated with the highest probability for brain/skull collision has not measurably changed. Furthermore, a comparison of these results with their 5.2 atm counterparts suggests that the ACH provides somewhat more effective protection at high blast peak pressures.

Spatial distribution of the maximum shear stress over the brain-lobe surfaces at a post-blast time at which this quantity experiences the largest value is displayed in Fig. 11(d). A comparison of the results displayed in Fig. 11(c, d) shows that a ca. 257% increase in the blast pressure led to a ca. 750% increase in the peak maximum surface-shear stress. Furthermore, a comparison of the results displayed in Fig. 11(b, d) shows that the addition of the ACH decrease the peak surface shear stress from 2.0 to 1.8 kPa (a ca. 10% change). This decrease is comparable to that seen in the 5.2 atm blast peak pressure case suggesting that ACH efficiency in reducing the probability of subdural hemorrhage-type TBI is not very pressure sensitive.

3.3 Shock-Wave Propagation/Reflection Analysis

The results presented in the previous section clearly established that the ACH helmet significantly reduces the ingress of shock waves into the intracranial cavity. While this finding is highly intuitive and expected, it is desirable to have a sound physics-based explanation of the observed blast-wave impact-mitigation effect. This would not only help explain the results obtained in the present work, but would help guide future development of the ACH protection systems. To provide the physical basis for the observed blast-wave impact-mitigation effect offered by the helmet, the pressure versus particle velocity Hugoniot curves are constructed and analyzed in this section. These curves were generated for all the attendant materials using the procedure described in our recent work (Ref 9) and are displayed in Fig. 14(a-d). Figure 14(a, b) are used for the unprotected-head case and for the two blast-wave peak-pressure levels, respectively. Figure 14(c, d) are used for the corresponding helmet-protected head cases. In each part of Fig. 14, the initial air-born blast-wave condition is indicated as Point 1.

The procedure described in our recent work (Ref 9) was next employed to determine the shock-wave pressure and the associated particle velocities at the skull/CSF interface (i.e., at the place of shock-wave ingress into the intracranial cavity). This procedure uses the equality of pressures and particle velocities in the two adjoining materials at the moment of shock-wave arrival to the interface between the materials and involves mirroring the Hugoniot curve of the material through which the shock wave was propagating before reaching the interface. Points 2, 3, etc. are used to denote the condition of the shock at different material interfaces. For example, Point 2 in Fig. 14(a, b) represents the shock condition at the air/skull interface, while Point 3 in the same figures represents the shock condition at the skull/CSF interface.

To quantify the blast-mitigation efficacy of the ACH, shockwaves at the skull/CSF interface are compared for the unprotected-head case [Point 3 in Fig. 14(a, b)] and the helmet-protected head case [Point 5 in Fig. 14(c, d)]. This comparison revealed that the ACH reduces the strength of the pressure shockwave entering the intra-cranial cavity at both levels of the blast peak pressure examined in the present work. Specifically, at the 5.2 atm blast peak-pressure level the ingress pressure-shock strength is reduced by ca. 6.1%, while at the 18.6 atm blast peak pressure level this reduction is ca. 4.5%. Since these reductions represent less than half of those reported in the previous section, it appears that additional shock-wave energy dissipation phenomena, not accounted for in the present shock-impedance analysis, accompany shock-wave propagation through the helmet/head assembly. Work is under way to identify and quantify these phenomena and the results obtained will be reported in our future communication.

4. Summary and Conclusions

Based on the results obtained in the present work, the following main summary remarks and conclusions can be drawn:

1. A comprehensive computational investigation of the collision between an air-borne blast wave and either an unprotected-head or a helmet-protected head was carried out. This entailed the construction of fairly detailed geometrical models for the helmet, the skull and several intracranial brain sections. In addition, detailed constitutive

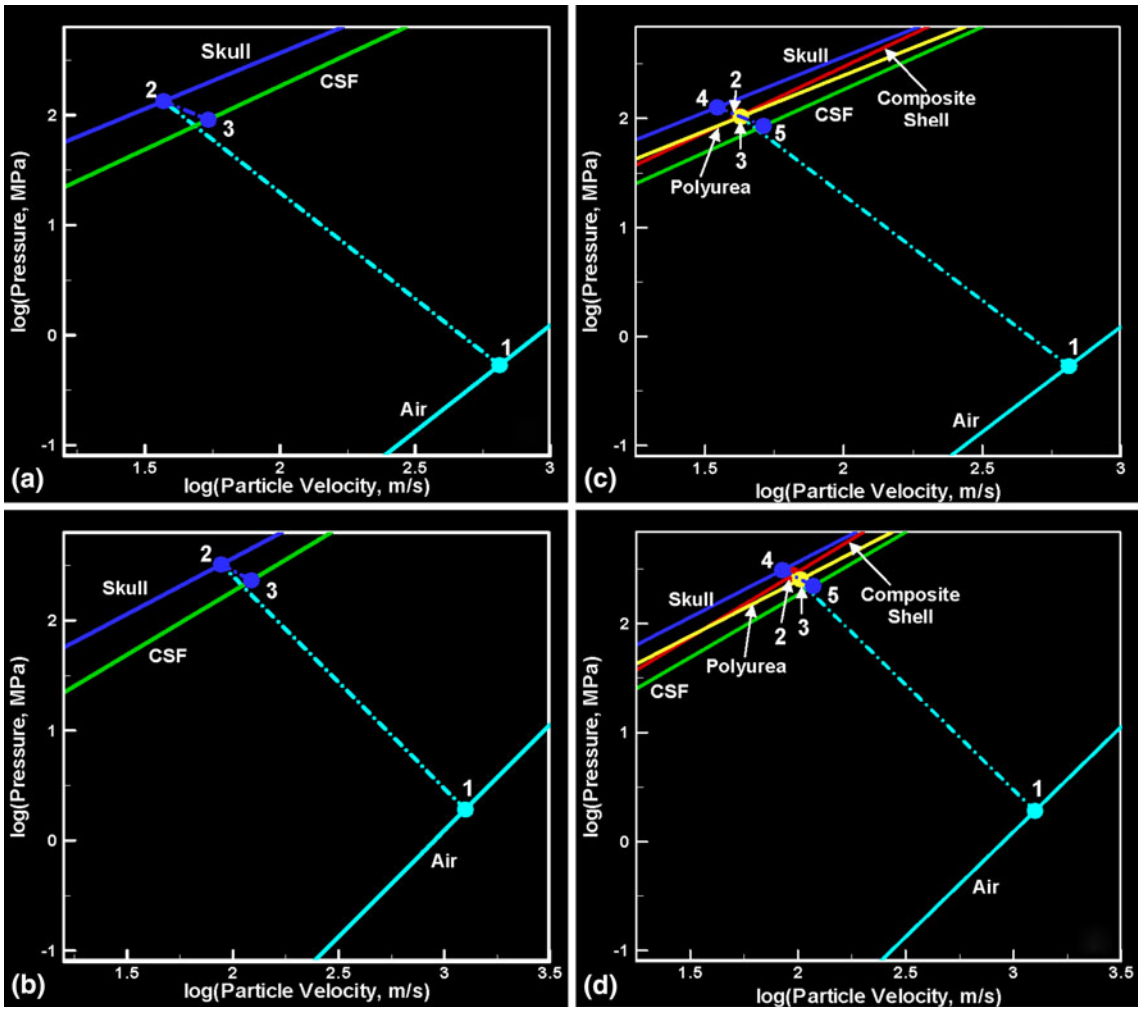

Fig. 14 Determination of the shock wave strength at the moment of its ingress into the intra-cranial cavity for unprotected-head case (a) and (b), protected-head case (c) and (d), 5.2 atm peak pressure (a) and (c) and 18.6 atm peak pressure (b) and (d)

models had to be identified and parameterized for a number of structural materials as well as for a number of hard and soft-tissue biological materials. Finally, the work involved modeling of the fluid/solid and solid/solid interactions.

2. The results obtained revealed impact-generated shock waves within the intra-cranial cavity consisting of longitudinal (normal stress-dominated) and transverse (shear stress-dominated) waves whose propagation and multiple reflections gave rise to very complex spatial distributions and temporal evolutions of stresses within the brain.
3. For the three most common types of mTBI, i.e., axonal damage, contusion, and subdural hemorrhage, an attempt was made to correlate the peak intra-cranial stresses (and the associated deformations) with the likelihood for occurrence of these types of mTBI.
4. The efficacy of an ACH head protection system in reducing the likelihood of blast-induced mTBI was investigated and it was found that an ACH provides some level of protection against all investigated types of mTBI and that the level of protection increases somewhat with an increase in blast peak pressure.
5. A shockwave propagation/reflection analysis was carried out in order to rationalize the aforementioned findings. This analysis qualitatively corroborated the results pertaining to the blast-mitigation efficacy of an ACH but also suggested that there are additional shockwave energy dissipation phenomena which play an important role in the mechanical response of the unprotected/protected head to blast impact.

Acknowledgments

The material presented in this article is based on work supported by the Office of Naval Research (ONR) research contract entitled "Elastomeric Polymer-By-Design to Protect the Warfighter Against Traumatic Brain Injury by Diverting the Blast Induced Shock Waves from the Head," Contract Number 4036-CU-ONR-1125 as funded through the Pennsylvania State University. The authors are indebted to Dr. Roshdy Barsoum of ONR for continuing support and interest in the present work and to professors J. Runt, J. Tarter, G. Settles, G. Dillon, and M. Hargether for stimulating discussions and friendship.

References

1. S. Okie, Traumatic Brain Injury in the War Zone, *N. Engl. J. Med.*, 2005, **352**, p 2043–2047
2. K.H. Taber, D.L. Warden, and R.A. Hurley, Blast-Related Traumatic Brain Injury: What is Known?, *J. Neuropsychiatr. Clin. Neurosci.*, 2006, **18**, p 141–145
3. S.J. Wallsten and K. Kosec, Social Science Research Network, Paper No. 05-19, http://ssrn.com/abstract=848408, 2005
4. Y. Bhattacharjee, Shell Shock Revisited: Solving the Puzzle of Blast Trauma, *Science*, 2008, **319**, p 406–408
5. D. Warden, Military TBI, During the Iraq and Afghanistan Wars, *J. Head Trauma Rehabil.*, 2006, **21**, p 398–402
6. I. Cernak, Z. Wang, J. Jiang, X. Bian, and J. Savic, Ultrastructural and Functional Characteristics of Blast Injury-Induced Neurotrauma, *J. Trauma Inj. Infect. Crit. Care*, 2001, **50**(4), p 695–706
7. L. Holm, J.D. Cassidy, L.J. Carroll, and J. Berg, Neurotrauma Task Force on Mild Traumatic Brain Injury of the WHO Collaborating Centre: Summary of the WHO Collaborating Centre for Neurotrauma Task Force on Mild Traumatic Brain Injury, *J. Rehabil. Med.*, 2005, **37**, p 131–141
8. S.M. Walsh, R.R. Scott, and D.M. Spagnuolo, *The Development of a Hybrid Thermoplastic Ballistic Material with Application to Helmets*, ARL-TR-3700, Army Research Laboratory, December 2005
9. M. Grujicic, W.C. Bell, B. Pandurangan, and T. He, Blast-Wave Impact-Mitigation Capability of Polyurea When Used as Helmet Suspension Pad Material, *J. Mater. Eng. Perform.*, 2010, **31**(9), p 4050–4065
10. M.R. Amini, A.V. Amirkhizi, and S. Namet-Naser, Numerical Modeling of Response of Monolithic and Bilayer Plates to Impulsive Loads, *Int. J. Impact Eng.*, 2010, **37**, p 90–102
11. Y.A. Bahei-El-Din, G.J. Dvorak, and O.J. Fredricksen, A Blast-Tolerant Sandwich Plate Design with a Polyurea Interlayer, *Int. J. Solids Struct.*, 2006, **43**, p 7644–7658
12. R.B. Bogoslovov, C.M. Roland, and R.M. Gamache, Impact-Induced Glass Transition in Elastomeric Coatings, *Appl. Phys. Lett.*, 2007, **90**, p 221910
13. I. Cullis, Blast Waves and How They Interact with Structures, *J. R. Army Med. Corps*, 2001, **147**(1), p 16–26
14. N. Kambouchev, L. Noels, and R. Radovitzky, Numerical Simulation of the Fluid-Structure Interaction Between Air Blast Waves and Free-standing Plates, *Comput. Struct.*, 2007, **23**, p 325–347
15. D.F. Moore, R. Radovitzky, L. Shupenko, A. Klinoff, M.S. Jaffee, and J.M. Rosen, Blast Physics and Central Nervous System Injury, *Future Neurol. Ann. Neurol.*, 2008, **64**, p S30
16. M. Grujicic, G. Arakere, and T. He, Material-Modeling and Structural-Mechanics Aspects of the Traumatic Brain Injury Problem, Multidiscipline Model. *Mater. Struct.*, 2009, **6**(1)
17. ABAQUS Version 6.8-1, User Documentation, Dassault Systems, 2008
18. Hypermesh, Altair Engineering, Inc., www.altair.com
19. ANSYS/Autodyn-2D and 3D, Version 6.1, User Documentation, ANSYS Inc., 2007
20. C.Y. Tham, V.B.C. Tan, and H.P. Lee, Ballistic Impact of a Kevlar® Helmet: Experiment and Simulations, *Int. J. Impact Eng.*, 2008, **35**, p 304–318
21. A.V. Amirkhizi, J. Isaacs, J. McGee, and S. Nemat-Nasser, An Experimentally-Based Viscoelastic Constitutive Model for Polyurea, Including Pressure and Temperature Effects, *Phil. Mag.*, 2006, **86**(36), p 5847–5866
22. A. Cuitiño and M. Ortiz, A Material-independent Method for Extending Stress Update Algorithms from Small-Strain Plasticity to Finite Plasticity with Multiplicative Kinematics, *Eng. Comput.*, 1992, **9**, p 437–451
23. ConWep Blast Simulation Software, US Army Corps of Engineers, Vicksburg, MS
24. M. Grujicic, B. Pandurangan, G. Arakere, W.C. Bell, T. He, and X. Xie, Musculoskeletal Computational Analysis of the Influence of Car-Seat Design/Adjustments on Long-distance Driving Fatigue, *Mater. Des.*, 2009, **30**, p 4273–4285
25. The Perspectives Network: Survive with Pride, Brain Map, http://www.tbi.org/html/brain_map.html
26. L. Zhang, K.H. Yang, R. Dwarampudi, K. Omori, T. Li, K. Chang, W.N. Hardy, T. Khalil, and A.I. King, Recent Advances in Brain Injury Research: A New Human Head Model Development and Validation, *Stapp Car Crash J.*, 2001, **45**, p 369–394
27. L. Zhang, K.H. Yang, and A.I. King, A Proposed Injury Threshold for Mild Traumatic Brain Injury, *J. Biomech. Eng.*, 2004, **126**, p 226–236